

New Computational Approach to Determine Liquid–Solid Phase Equilibria of Water Confined to Slit Nanopores

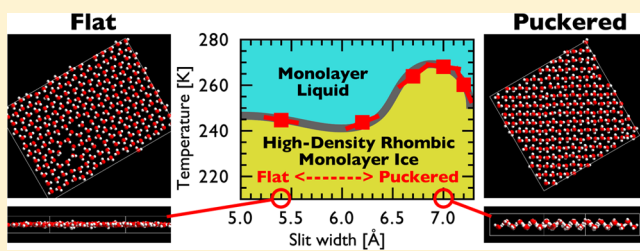
Toshihiro Kaneko,[†] Jaeil Bai,[‡] Kenji Yasuoka,^{*,†} Ayori Mitsutake,[§] and Xiao Cheng Zeng^{*,‡}

[†]Department of Mechanical Engineering, Keio University, Yokohama, 223-8522, Japan

[‡]Department of Chemistry, University of Nebraska-Lincoln, Lincoln, Nebraska 68588, United States

[§]Department of Physics, Keio University, Yokohama, 223-8522, Japan

ABSTRACT: We devise a new computational approach to compute solid–liquid phase equilibria of confined fluids. Specifically, we extend the multibaric–multithermal ensemble method with an anisotropic pressure control to achieve the solid–liquid phase equilibrium for confined water inside slit nanopores (with slit width h ranging from 5.4 Å to 7.2 Å). A unique feature of this multibaric–multithermal ensemble is that the freezing points of confined water can be determined from the heat-capacity peaks. The new approach has been applied to compute the freezing point of two monolayer ices, namely, a high-density flat rhombic monolayer ice (HD-fRMI) and a high-density puckered rhombic monolayer ice (HD-pRMI) observed in our simulation. We find that the liquid-to-solid transition temperature (or the freezing point) of HD-pRMI is dependent on the slit width h , whereas that of HD-fRMI is nearly independent of the h .



1. INTRODUCTION

Confined water in nanoscale pores is ubiquitous in nature, for example, in biological cell systems,^{1,2} minerals,^{3–6} and microporous materials.^{7–35} When the confined water is slowly cooled, new forms of nanoice may arise under certain conditions, such as the formation of ice nanotubes/nanowires within carbon nanotubes^{8–13} and the formation of ice nanosheets.^{14–23} Moreover, previous experiments have shown that the freezing temperature (or the freezing point) of water confined to porous silica,^{24–26} carbon nanotubes,^{9,13,27} or activated carbon fiber^{28,29} can be shifted to either a higher or lower temperature, compared to the bulk ice. In addition to their scientific importance, these nanopores are potentially used as an inhibitor or a promoter of ice formation, or as a medium for energy storage.^{36,37} Therefore, it is important to understand mechanism of the depression/elevation of the freezing temperature of water within nanopores and to obtain the liquid–solid phase equilibria of the highly confined water.

Slit nanopores made of two parallel flat surfaces are commonly used as a prototype model system to study effects of nanoscale confinement on the phase behavior of confined fluids. Previous molecular simulations based on this type of model system have predicted several two-dimensional (2D) crystalline ice or amorphous ice structures, such as the bilayer hexagonal ice (bilayer ice I)^{7,8,20,23} consisting of rows of distorted hexagons,¹⁴ a bilayer amorphous ice,^{15,16} a high-density rhombic monolayer ice (HD-RMI),^{17–19,21} a low-density 4-8² monolayer ice (LD-48MI),²¹ and bilayer very high density amorphous (BL-VHDA) ices.^{16,23} According to the Gibbs' phase rule, at the phase equilibrium, a one-component system under a given pressure should possess a unique temperature at which the solid and liquid phases have the same Gibbs free

energy. For bulk ice, this temperature is known as the freezing point of the system at the given pressure. The pressure-dependent freezing points give rise to the liquid–solid phase equilibria. Although a number of 2D nanoices have been reported in the literature, the freezing points of most nanoices are only estimated within the range of a hysteresis typically observed in heating/cooling simulations.^{15,16,19} So this approach cannot give precise freezing points due to the uncertainty of 20–30 K (hysteresis). To determine the freezing points more quantitatively, the free-energy calculation method³⁸ or the two-phase coexistence method³⁹ has been used. However, both methods require a candidate crystalline structure as an initial input, which may not be the most stable crystalline structure in the slit nanopores.

One possible way to mitigate this difficulty is the development of the multicanonical (MUCA) and multibaric–multithermal (MUBATH) ensemble approaches. In MUCA, an artificial potential energy is introduced such that a wide range of potential energy surface can be sampled without having the system trapped in local minima, and the most stable crystalline structure is formed spontaneously without examining various crystalline structures as the initial input. MUBATH^{40,41} is an extension of the MUCA approach to realize 2D random walks on both the potential-energy space and the volume space. These ensembles have been applied to address various challenging problems, such as protein folding and spin glass (for reviews, see refs 42–44, and for a generalized formulation for multidimensional version, see refs 45 and 46). The primary advantage of these ensembles is that more than one phase can be visited within a single simulation run, and thus, the states

Received: March 19, 2013

Published: June 18, 2013



near the phase transition can be determined in detail. Such an MUCA approach has been applied to determine the liquid–solid^{47,48} and liquid–gas⁴⁹ phase equilibria of the Lennard-Jones (LJ) system and to study structural transitions in water clusters.⁵⁰ The phase equilibrium conditions for these systems have been quantitatively obtained. Because MUCA and MUBATH ensembles are only available under the constant volume and isotropic pressure control, respectively, few studies have been reported for the determination of the freezing point of low-dimensional solids, which requires an anisotropic pressure control. In this work, we develop a new MUBATH ensemble approach that involves an anisotropic pressure control. As an application of this newly developed approach, we determine the phase equilibrium conditions for the 2D HD-RMI and 2D water confined to a slit nanopore with various width h .

2. THEORY

2.1. Multibaric–Multithermal Ensemble. Here, we briefly summarize the MUBATH method. More theoretical details can be found in the original papers.^{40,41} In the conventional isobaric–isothermal ensemble, the distribution of potential energy E and volume V at a given temperature T_0 and pressure P_0 is given by

$$F_{\text{NPT}}(E, V) \propto n(E, V) \exp[-\beta_0(E + P_0V)] \quad (1)$$

where $n(E, V)$ is the density of states and $\beta_0 = 1/k_B T_0$. This ensemble has a bell-shaped distribution in either E or V at the given T_0 and P_0 and $\exp[-\beta_0(E + P_0V)]$ is known as the Boltzmann factor.

In the MUBATH method, the artificial weight factor (rather than the Boltzmann factor) is used, that is,

$$W_{\text{MUBATH}} = \exp[-\beta_0 H_{\text{MUBATH}}(E, V; T_0, P_0)] \quad (2)$$

so that a uniform distribution $F_{\text{MUBATH}}(E, V)$ may be obtained:

$$\begin{aligned} F_{\text{MUBATH}}(E, V) &\propto n(E, V) \exp[-\beta_0 H_{\text{MUBATH}}(E, V; T_0, P_0)] \\ &\equiv \text{Const} \end{aligned} \quad (3)$$

Here, W_{MUBATH} and $H_{\text{MUBATH}}(E, V; T_0, P_0)$ are referred to as the MUBATH weight factor and the MUBATH enthalpy, respectively. From eq 3, we find

$$H_{\text{MUBATH}}(E, V; T_0, P_0) \propto k_B T_0 \ln n(E, V) \quad (4)$$

In the MUBATH method, one can set

$$H_{\text{MUBATH}}(E, V; T_0, P_0) = E + P_0 V + \delta H(E, V; T_0, P_0) \quad (5)$$

Before performing a long production run, we need to determine the MUBATH weight factor (i.e., $\delta H(E, V; T_0, P_0)$) so that $F_{\text{MUBATH}}(E, V)$ could be flat over a wide range of E and V from some short simulations (see section 3 for the determination processes for the systems in this article). Once we obtain an appropriate $\delta H(E, V; T_0, P_0)$, a molecular dynamics simulation based on $H_{\text{MUBATH}} = H + \delta H(E, V; T_0, P_0)$ instead of $H = E + P_0 V$ can realize random walks on the E and V surface and sample numerous states over a wide range of E and V (in the article, states include both solid and liquid phases).

After the long production run, we can obtain an averaged physical property at any T and P by using the reweighting techniques. From the flat distribution $F_{\text{MUBATH}}(E, V)$ obtained by the long production run with the weight factor

$\exp[-\beta_0 H_{\text{MUBATH}}(E, V; T_0, P_0)]$, $n(E, V)$ in the given wide range of E and V can be estimated by using the formula:

$$n(E, V) \propto F_{\text{MUBATH}}(E, V) \exp[\beta_0 H_{\text{MUBATH}}(E, V; T_0, P_0)] \quad (6)$$

The average physical property $A(E, V)$ at the given T and P is calculated by

$$\langle A \rangle_{T,P} = \frac{\sum_{E,V} A(E, V) n(E, V) e^{-\beta(E+PV)}}{\sum_{E,V} n(E, V) e^{-\beta(E+PV)}} \quad (7)$$

In this paper, $\langle \dots \rangle_{T,P}$ denotes the ensemble average defined by eq 7. We calculate the average potential energy $\langle E \rangle_{T,P}$ and the average volume $\langle V \rangle_{T,P}$, among others. The isobaric heat capacity is calculated using the equation

$$C_P(T) = \frac{\langle H^2 \rangle_T - \langle H \rangle_T^2}{k_B T^2} + 3Nk_B \quad (8)$$

where $H = E + PV$ is enthalpy. During a MUBATH production run, a load pressure $P_{\text{wall}}(E, V)$, which is the total force from the walls divided by the area, is recorded. The average load pressure $\langle P_{\text{wall}} \rangle_{T,P}$ is also computed by eq 7.

2.2. Equations of Motion for Anisotropic Pressure Control. Based on the Nosé–Andersen method, we propose a new MUBATH ensemble method for the anisotropic pressure control. First, p_i and r_i are vectors of the momentum and coordinate of particle i , respectively.

$$p_i = \begin{pmatrix} p_{xi} \\ p_{yi} \\ p_{zi} \end{pmatrix} \quad r_i = \begin{pmatrix} x_i \\ y_i \\ z_i \end{pmatrix} \quad (9)$$

Then, $\mathbf{p}^N = (p_1, p_2, \dots, p_N)$ and $\mathbf{r}^N = (r_1, r_2, \dots, r_N)$ are matrices of all particles' momenta and positions, respectively. The simulation cell is rectangular parallelepiped, whose size is $V = l_x l_y l_z$. The matrix L and inverse matrix L^{-1} are defined by

$$L = \begin{pmatrix} l_x & 0 & 0 \\ 0 & l_y & 0 \\ 0 & 0 & l_z \end{pmatrix} \quad L^{-1} = \begin{pmatrix} 1/l_x & 0 & 0 \\ 0 & 1/l_y & 0 \\ 0 & 0 & 1/l_z \end{pmatrix} \quad (10)$$

The normalized momentum \tilde{p}_i and position \tilde{r}_i are

$$\tilde{p}_i = L p_i = \begin{pmatrix} l_x p_{xi} \\ l_y p_{yi} \\ l_z p_{zi} \end{pmatrix} \quad \tilde{r}_i = L^{-1} r_i = \begin{pmatrix} x_i/l_x \\ y_i/l_y \\ z_i/l_z \end{pmatrix} \quad (11)$$

We define s as the variable of thermostat for Nosé method. Then, the virtual time $t' = st$ and virtual momentum $p'_i = sp_i$ and $\tilde{p}'_i = s\tilde{p}_i$ are introduced.

In the original MUBATH^{40,41} method, the Hamiltonian \mathcal{H}_0 is introduced based on an isotropic pressure control,

$$\begin{aligned} \mathcal{H}_0(\tilde{p}'^N, \tilde{r}^N, \pi_V, V, \pi_s, s) &= \sum_{i=1}^N \frac{(L^{-1}\tilde{p}'_i)^2}{2m_i s^2} + E(L\tilde{r}^N) + \frac{\pi_V^2}{2M_V} + \frac{\pi_s^2}{2Q} \\ &+ gk_B T_0 \ln s + P_0 V + \delta H(E(L\tilde{r}^N), V) \end{aligned} \quad (12)$$

where the volume $V = l_x l_y l_z$; π_V and M_V are the momentum and mass of barostat, respectively; and π_s and Q are the momentum

Table 1. Parameters for MUBATH Simulations

h [Å]	P_0 [MPa]	T_0 [K]
5.4	200	240
6.2	200	250
6.7	200	260
7.0	200	260
7.2	200	250

and mass of thermostat, respectively. Next, the equations of motion are derived in a manner of canonical equation.

In the new approach, we introduce a new Hamiltonian \mathcal{H} based on an anisotropic pressure control (see ref 51):

$$\begin{aligned} \mathcal{H}(\tilde{p}'^N, \tilde{r}^N, \pi_x, l_x, \pi_y, l_y, \pi_z, l_z, \pi_s, s) \\ = \sum_{i=1}^N \frac{(L^{-1}\tilde{p}_i')^2}{2m_i s^2} + E(L\tilde{r}^N) + \frac{\pi_x^2}{2M_x} + \frac{\pi_y^2}{2M_y} + \frac{\pi_z^2}{2M_z} \\ + \frac{\pi_s^2}{2Q} + gk_B T_0 \ln s + P_0 l_x l_y l_z + \delta H(E(L\tilde{r}^N), l_x l_y l_z) \end{aligned} \quad (13)$$

Here, we introduce $\pi_x, \pi_y, \pi_z, M_x, M_y$ and M_z , instead of π_V and M_V . We now derive the canonical equations of motion based on \mathcal{H} ,

$$\frac{d\tilde{r}_i}{dt'} = \frac{\partial \mathcal{H}}{\partial \tilde{p}_i'} = \frac{(L^{-1})^2 \tilde{p}_i'}{m_i s^2} \quad (14)$$

$$\frac{d\tilde{p}_i'}{dt'} = -\frac{\partial \mathcal{H}}{\partial \tilde{r}_i} = -\left(1 + \frac{\partial \delta H}{\partial E}\right) \frac{\partial E}{\partial \tilde{r}_i} \quad (15)$$

$$\frac{dl_x}{dt'} = \frac{\partial \mathcal{H}}{\partial \pi_x} = \frac{\pi_x}{M_x} \quad (16)$$

$$\begin{aligned} \frac{d\pi_x}{dt'} &= -\frac{\partial \mathcal{H}}{\partial l_x} \\ &= \frac{1}{l_x} \left[\left(\sum_{i=1}^N \frac{\tilde{p}_{ix}^2}{m_i l_x^2 s^2} \right) - \left(1 + \frac{\partial \delta H}{\partial E}\right) \left(\sum_{i=1}^N \frac{\partial E}{\partial x_i} x_i \right) - \left(P_0 + \frac{\partial \delta H}{\partial V}\right) l_x l_y l_z \right] \end{aligned} \quad (17)$$

$$\frac{ds}{dt'} = \frac{\partial \mathcal{H}}{\partial \pi_s} = \frac{\pi_s}{Q} \quad (18)$$

$$\frac{d\pi_s}{dt'} = -\frac{\partial \mathcal{H}}{\partial s} = \left[\sum_{i=1}^N \frac{(L^{-1}\tilde{p}_i')^2}{m_i s^3} \right] - \frac{gk_B T_0}{s} \quad (19)$$

Equations associated with dl_y/dt' , $d\pi_y/dt'$, dl_z/dt' , and $d\pi_z/dt'$ can be derived in the same way as for l_x and π_x . To derive eq 17, we need to use the equation

$$\frac{\partial E(L\tilde{r}^N)}{\partial l_x} = \sum_{i=1}^N \frac{\partial E}{\partial x_i} \frac{\partial x_i}{\partial l_x} = \sum_{i=1}^N \frac{\partial E}{\partial x_i} \tilde{x}_i = \frac{1}{l_x} \sum_{i=1}^N \frac{\partial E}{\partial x_i} x_i \quad (20)$$

Then, using the relations $dt' = s dt$ and $p'_i = sp_i$, we can convert virtual time t' to real time dt ,

$$\frac{d\tilde{r}_i}{dt} = \frac{(L^{-1})^2 \tilde{p}_i}{m_i} \quad (21)$$

$$\frac{d\tilde{p}_i}{dt} = -\left(1 + \frac{\partial \delta H}{\partial E}\right) \frac{\partial E}{\partial \tilde{r}_i} - \frac{\tilde{p}_i}{s} \frac{ds}{dt} \quad (22)$$

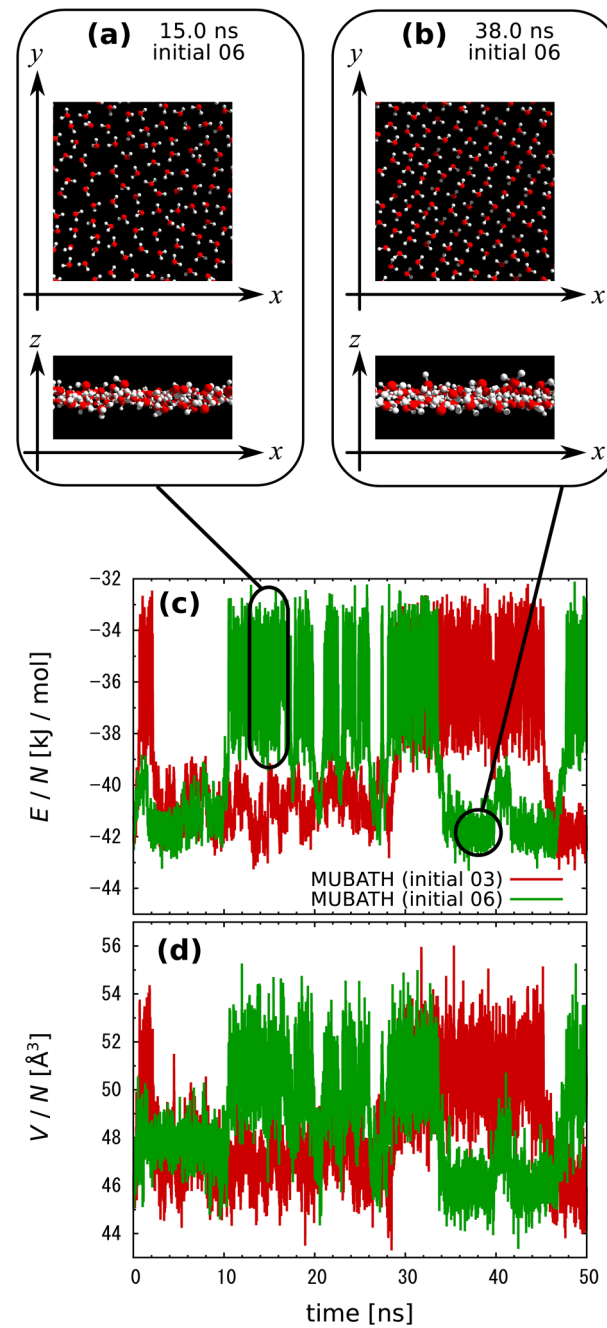


Figure 1. Snapshots of a liquid structure (a) and a solid structure (b) and time series of potential energy (c) and volume (d) obtained by MUBATH simulations of $h = 7.0$ Å. The time series of two different initial conditions, initial 03 and initial 06 are colored in red and green, respectively. Both liquid and solid structures are sampled in the course of the single MUBATH simulation.

$$\frac{dl_x}{dt} = s \frac{\pi_x}{M_x} \quad (23)$$

$$\frac{d\pi_x}{dt} = \frac{s}{l_x} \left[\left(\sum_{i=1}^N \frac{\tilde{p}_{ix}^2}{m_i l_x^2} \right) - \left(1 + \frac{\partial \delta H}{\partial E}\right) \left(\sum_{i=1}^N \frac{\partial E}{\partial x_i} x_i \right) - \left(P_0 + \frac{\partial \delta H}{\partial V}\right) l_x l_y l_z \right] \quad (24)$$

$$\frac{ds}{dt} = s \frac{\pi_s}{Q} \quad (25)$$

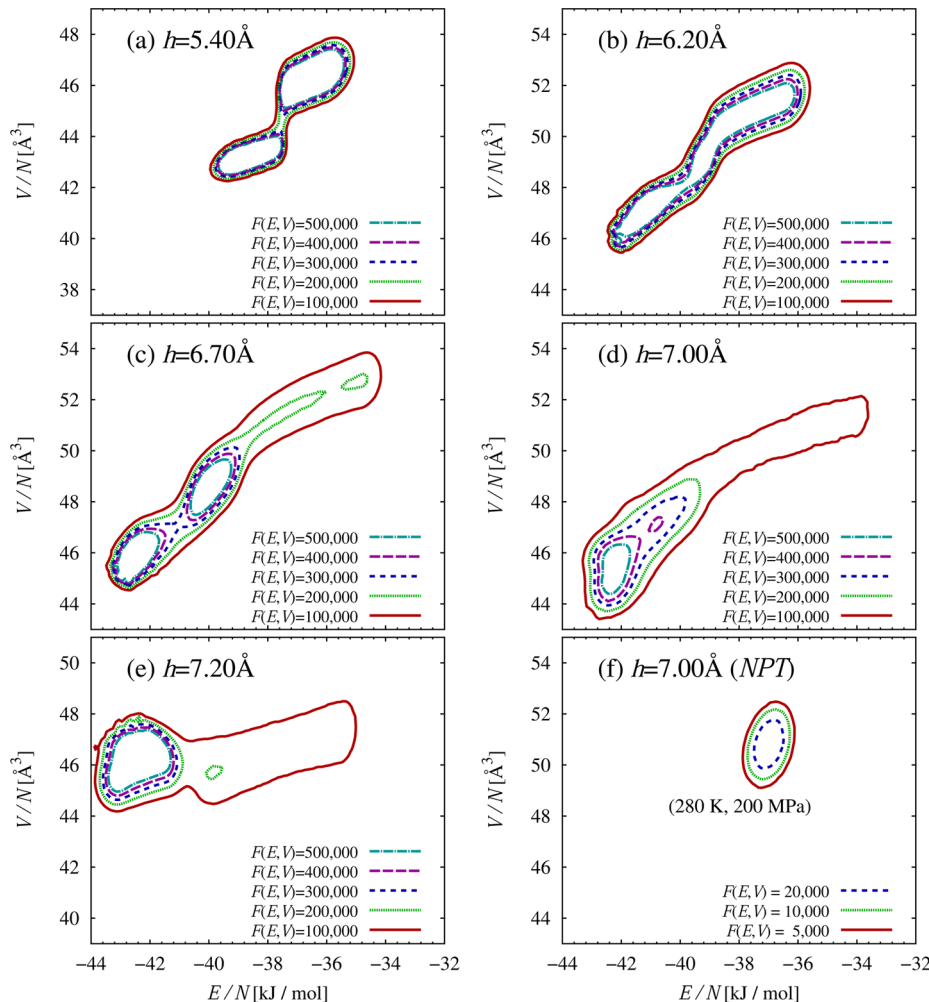


Figure 2. Contour plots of distributions of potential energy E and volume V , $F(E,V)$, in MUBATH ensembles (a–e) and a conventional isobaric–isothermal ensemble (f). It is confirmed that a flat distribution of $F(E,V)$ over a wide range of E and V is achieved, compared to that from the isobaric–isothermal ensemble, and within the range E and V , $n(E,V)$ is properly estimated.

$$\frac{d\pi_s}{dt} = \left[\sum_{i=1}^N \frac{(L^{-1}\tilde{p}_i)^2}{m_i} \right] - gk_B T_0 \quad (26)$$

For the slit nanopore systems considered in this study, π_z is always zero while l_z is a constant. Hence, the specific ensemble is denoted as the $NP_{xx}P_{yy}hT$ ensemble. To solve eq 21–eq 26, we have developed our own source code based on Nosé–Hoover–Andersen method with modifications by Ilnytskyi and Wilson.⁵²

3. SIMULATION SYSTEMS

The TIP4P⁵³ water model is adopted, and the wall model is the 9–3 Lennard-Jones potential given by $U_{\text{wall}-\text{O}}(z) = C_9/z^9 - C_3/z^3$. The parameters for describing interactions between water and hydrophobic surface^{19,54} are $C_9 = 17447.5\text{ \AA}^9\text{ kJ/mol}$ and $C_3 = 76.1496\text{ \AA}^3\text{ kJ/mol}$. The coulomb interaction among TIP4P models is calculated by Ewald summation in which the Ewald parameters are chosen such that the total potential energy values agree with the direct summation under 2D periodic boundary condition and within 10^{-4} in relative value.

All the simulations are performed based on the $NP_{xx}P_{yy}hT$ ensemble with $N = 200$. In previous studies, one of three methods of pressure control for molecules confined in nanoporous materials is typically used, namely: (i) attaching a bulk

reservoir,^{22–25} (ii) fluctuating h while fixing L_x and L_y ,^{14,55,56} and (iii) fluctuating L_x and L_y while fixing h .^{15,19,21} In the present study, relatively large sized crystals are needed to compute physical properties correctly. The method (i) is not applicable for this purpose because the periodic boundary conditions cannot be applied to the confined water. Also we want to study the liquid–solid transition in nanopores with specific width h , and thus the method (ii) is not applicable. Therefore, only the method (iii) is adopted and as such, the $NP_{xx}P_{yy}hT$ ensembles are used.

The integration is undertaken by using the velocity–Verlet method with SHAKE/RATTLE where the time step is 1 fs. To avoid shrinking of the simulation cell during the simulation, we implement the condition that if l_x or l_y become less than 25 Å, the barostat toward x or y , respectively, is stopped and then reset. After resetting of the barostat, samples of initial 10 ps are also excluded from the histogram $F(E,V)$. In addition to the MUBATH simulations, direct cooling/heating simulations with 5 K/0.5 ns are also performed in the conventional isobaric–isothermal ensemble as a reference data.

An appropriate MUBATH weight factor $\delta H(E,V;T_0,P_0)$ is determined by two or three iterations described below. $\delta H(E,V;T_0,P_0)$ is divided into two parts, that is, $\delta H(E,V;T_0,P_0) = \delta E(E;T_0,P_0) + \delta H^*(E,V;T_0,P_0)$. (i) We can make a rough estimate

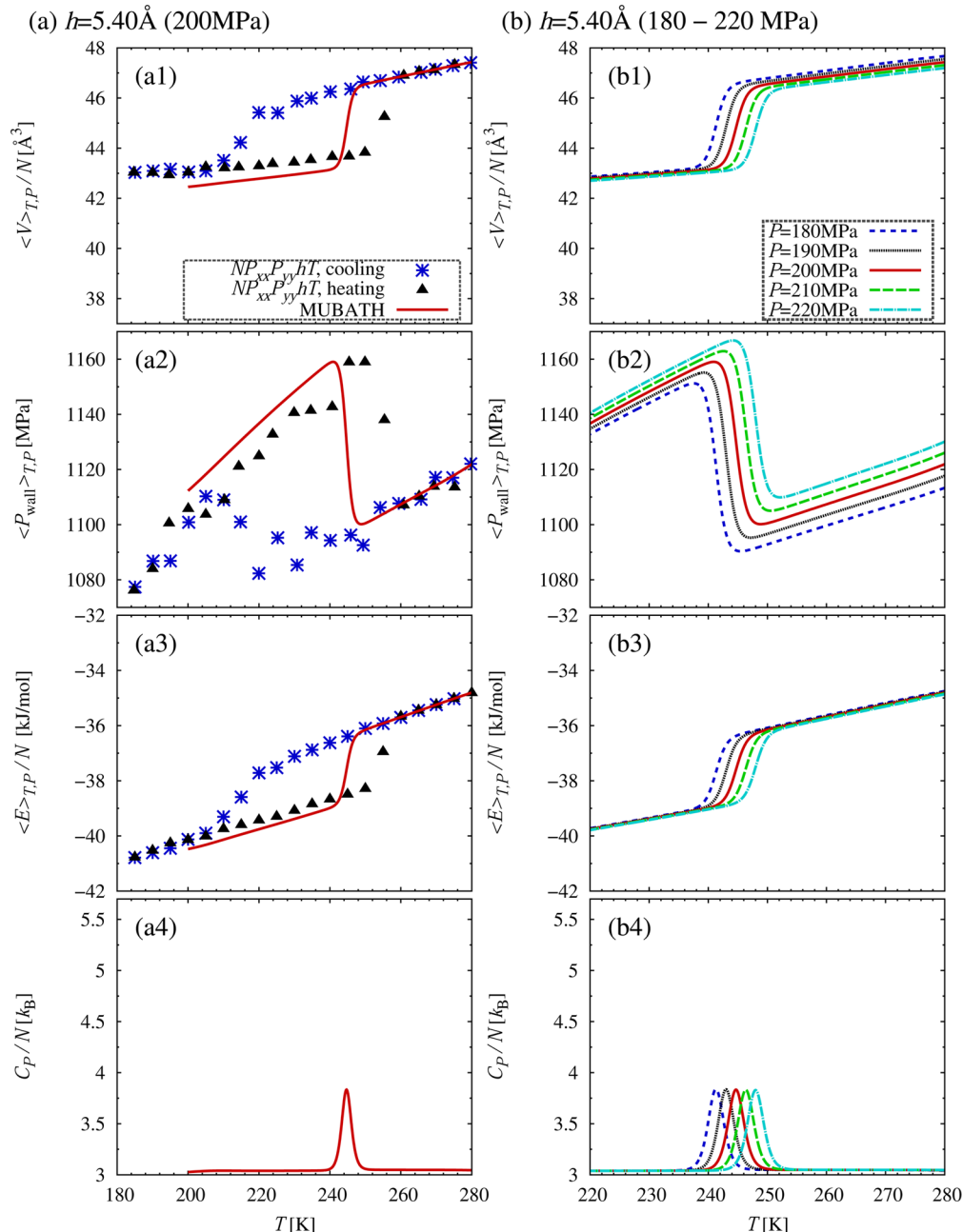


Figure 3. Average volume $\langle V \rangle_{T,P}$, the average load pressure $\langle P_{\text{wall}} \rangle_{T,P}$, the average potential energy $\langle E \rangle_{T,P}$ and the isobaric heat capacity $C_p(T,P)$ are calculated by using eqs 7 and 8. (a1–a4) Results at $P_{xx} = 200$ MPa obtained by the MUBATH simulation and reweighting techniques and cooling/heating simulations in conventional isobaric–isothermal ensembles. (b1–b4) Corresponding results at $P_{xx} = 180, 190, 200, 210$, and 220 MPa.

of $\delta E(E; T_0, P_0)$ by using isobaric–multithermal ensemble⁵⁷ and Wang–Landau method.^{49,58} (ii) $\delta H^*(E, V; T_0, P_0)$ is estimated by using the MUBATH ensemble and Wang–Landau method based on $\delta E(E; T_0, P_0)$. (iii) A short MUBATH production run is performed using $\delta E(E; T_0, P_0)$ and $\delta H^*(E, V; T_0, P_0)$, and rough $n(E, V)$ data are obtained. (iv) Using the relation

$$\delta E(E; T_0, P_0) = k_B T_0 \ln [\int n(E, V) \exp(-\beta_0 P_0 V) dV] - E \quad (27)$$

an improved weight factor $\delta E(E; T_0, P_0)$ is obtained. Then, we return to procedure step ii. Note that eq 27 is derived from eq 27 of ref 57. The procedure steps ii, iii, and iv are iterated until an appropriate MUBATH weight factor is achieved. After an appropriate MUBATH weight factor is attained, we perform

50 ns MUBATH simulations with eight different initial conditions (four liquid initial conditions and four solid initial conditions) as a production run. The MUBATH parameters P_0 and T_0 for the production runs are summarized in Table 1. A total of 400 ns of $F(E, V)$ are used for analysis.

4. RESULTS AND DISCUSSION

4.1. Average Physical Properties Computed from Multibaric–Multithermal Ensemble. Time series of the potential energy E and volume V for $h = 7.0$ Å are shown in Figure 1. Two different initial conditions are colored in red and green. Random walk behavior between the liquid and solid states are observed in the course of each simulation, which implies a sensible MUBATH weight factor $\delta H(E, V)$ is estimated

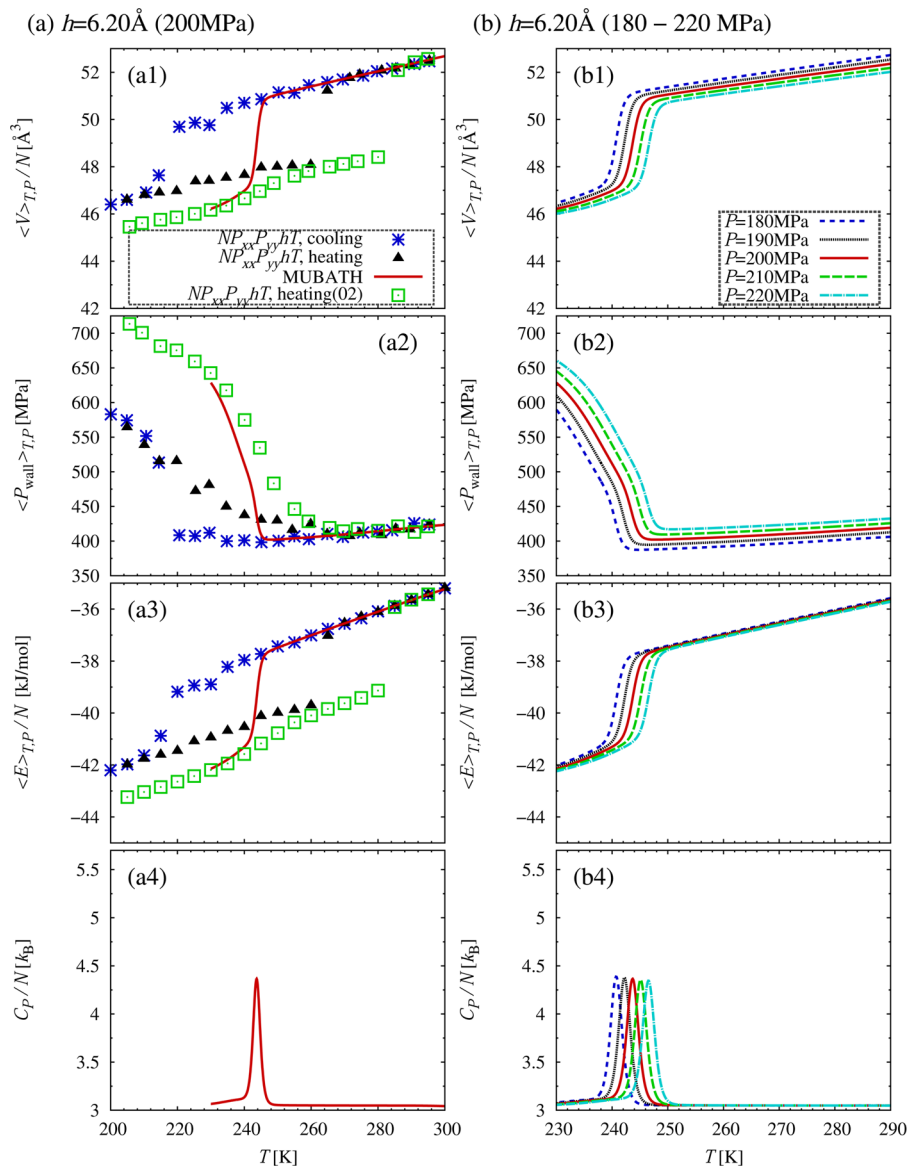


Figure 4. Results for $h = 6.2 \text{ \AA}$. For details, see the caption of Figure 3. In the course of MUBATH simulations, a lower-energy ice is observed compared to the cooling simulations. Using this low-energy ice as an initial condition, additional heating simulation is performed. The results are plotted in green squares.

for the study of liquid–solid transitions. In Figure 2, the contour lines of the distribution of potential energy and volume $F(E,V)$ in MUBATH ensembles (Figure 2a–e) and a conventional isobaric–isothermal ensemble (Figure 2f) are shown. The distribution in MUBATH ensembles is broader than that in the conventional isobaric–isothermal ensemble. In Figure 2a–e, nearly flat distributions of $F(E,V)$ over a wide range of E and V are seen.

To attain appropriate $F(E,V)$ for each given h in the MUBATH ensemble, about 400 ns simulation is needed. A typical range of simulation time to determine one freezing point is 100–1000 ns (500 water molecules) using the free energy calculation method³⁸ and about 10 ns (12288 water molecules) using the two-phase coexistence method.³⁹ Although the MUBATH ensemble approach is not computationally the fastest, a major advantage of this approach is that the most stable crystalline structure and system structures near the freezing point could be unbiasedly searched without relying on initial conditions, as described in Figure 1.

Once appropriate $n(E,V)$ over the desired wide range of E and V is obtained, the average volume $\langle V \rangle_{T,P}$, the load pressure $\langle P_{\text{wall}} \rangle_{T,P}$, the potential energy $\langle E \rangle_{T,P}$ and the isobaric heat capacity $C_p(T)$ are computed using eqs 7 and 8. These are summarized in Figures 3–7. In each figure, isobaric curves at 200 MPa obtained by reweighting techniques and heating/cooling are summarized in a1–a4. Isobaric curves at 180, 190, 200, 210, and 220 MPa obtained by reweighting techniques are summarized in b1–b4. In all the cases, a sharp peak in $C_p(T)$ and discontinuous changes in $\langle V \rangle_{T,P}$, $\langle P_{\text{wall}} \rangle_{T,P}$, and $\langle E \rangle_{T,P}$ are observed, and all suggest a first-order phase transition. We define the temperature corresponding to the peak in heat-capacity curves as the liquid-to-solid transition temperature, and this temperature is between the freezing temperature shown in the cooling simulation and the melting temperature shown in the heating simulation.

In all the cases, the results of MUBATH ensembles are consistent with those of heating/cooling simulations in the liquid region (or high-temperature region). In some cases, the results

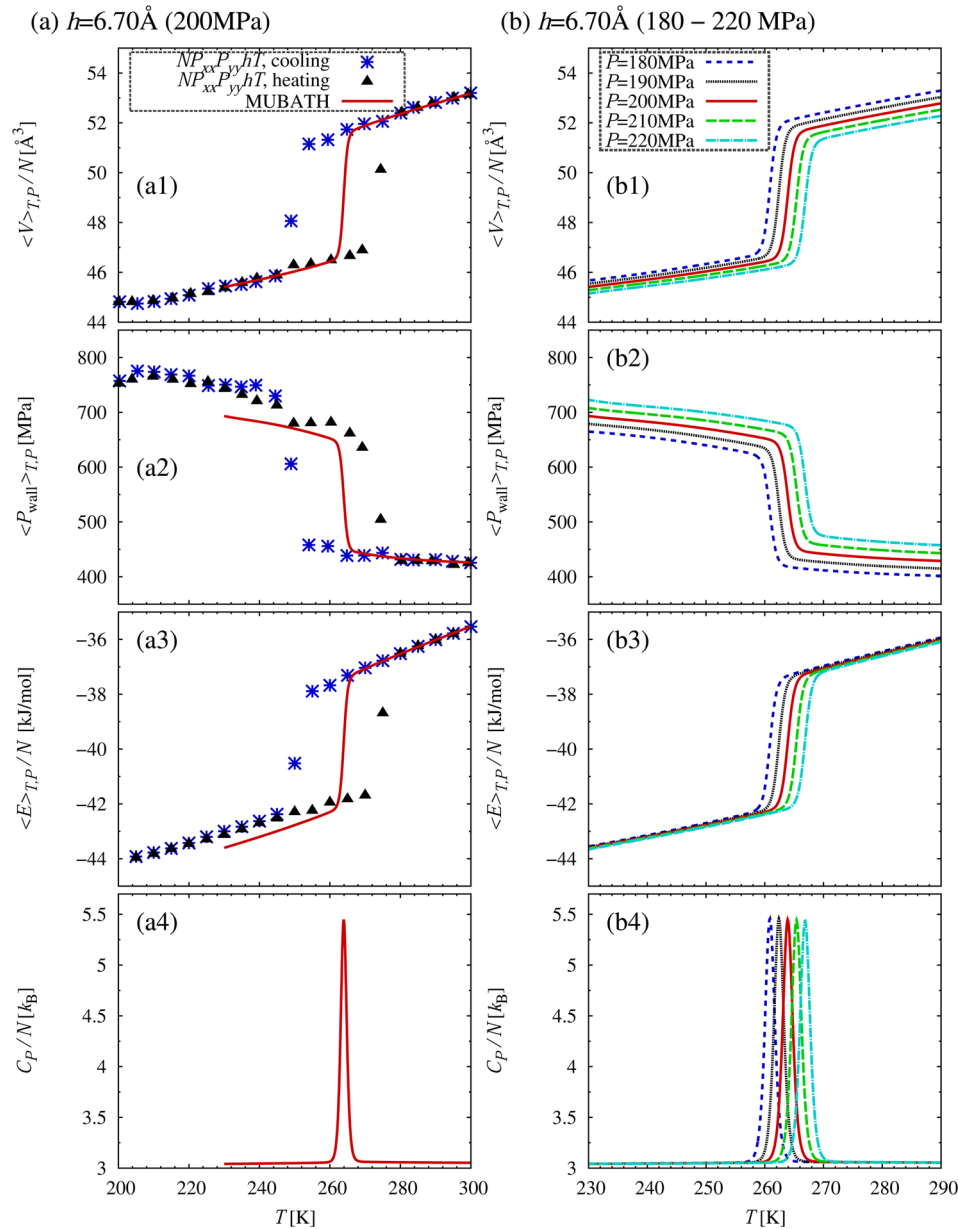


Figure 5. Results for $h = 6.7 \text{ \AA}$. For details, see the caption of Figure 3.

of MUBATH ensembles are different from those of cooling simulations in the solid region (or low-temperature region), especially in Figure 4a1–a3 and Figure 6a2. A cooling simulation is just a single cooling event, whereas the MUBATH ensembles involve multiple times of cooling events, and thus, an average value of many solid structures is obtained. The consistency between independent simulations suggests that the MUBATH ensembles give reliable information. In a3 of Figures 3–7, the solid structures predicted from the MUBATH ensembles show lower potential energies than those of direct cooling simulations. That means more stable structures can be achieved by the MUBATH ensembles than cooling simulations.

For $h = 6.2 \text{ \AA}$, a big difference between the cooling simulation and MUBATH ensembles is observed. A cooling simulation generates a high-energy monolayer ice, but the MUBATH ensembles generate a low-energy monolayer ice. To check validity of the results of the MUBATH ensembles, an additional heating simulation is performed starting from the low-energy

ice obtained in the MUBATH ensembles and plotted as heating (02) in Figure 4. Although there is a difference in transition temperature, heating (02) and the MUBATH ensembles give consistent results. It is also confirmed that the low-energy ice exists in the $NP_{xx}P_{yy}hT$ ensemble, and therefore, the high-energy ice is a metastable structure for $h = 6.2 \text{ \AA}$.

4.2. Liquid-to-Solid Transition Conditions and Phase Diagram.

The liquid-to-solid transition temperature at 200 MPa is determined from the peak value of the heat capacity curve in a4 of Figures 3–7. The temperature versus the slit width ($T-h$) phase diagram is summarized in Figure 8c. We also calculate the slopes of the liquid–solid equilibrium surface in the $T-P_{xx}-h$ thermodynamic space, using the Clausius–Clapeyron equation for the slit system:¹⁹

$$\left(\frac{\partial T}{\partial P_{xx}} \right)_h = \frac{hT(a^L - a^S)}{u^L - u^S + (a^L - a^S)hP_{xx}} \quad (28)$$

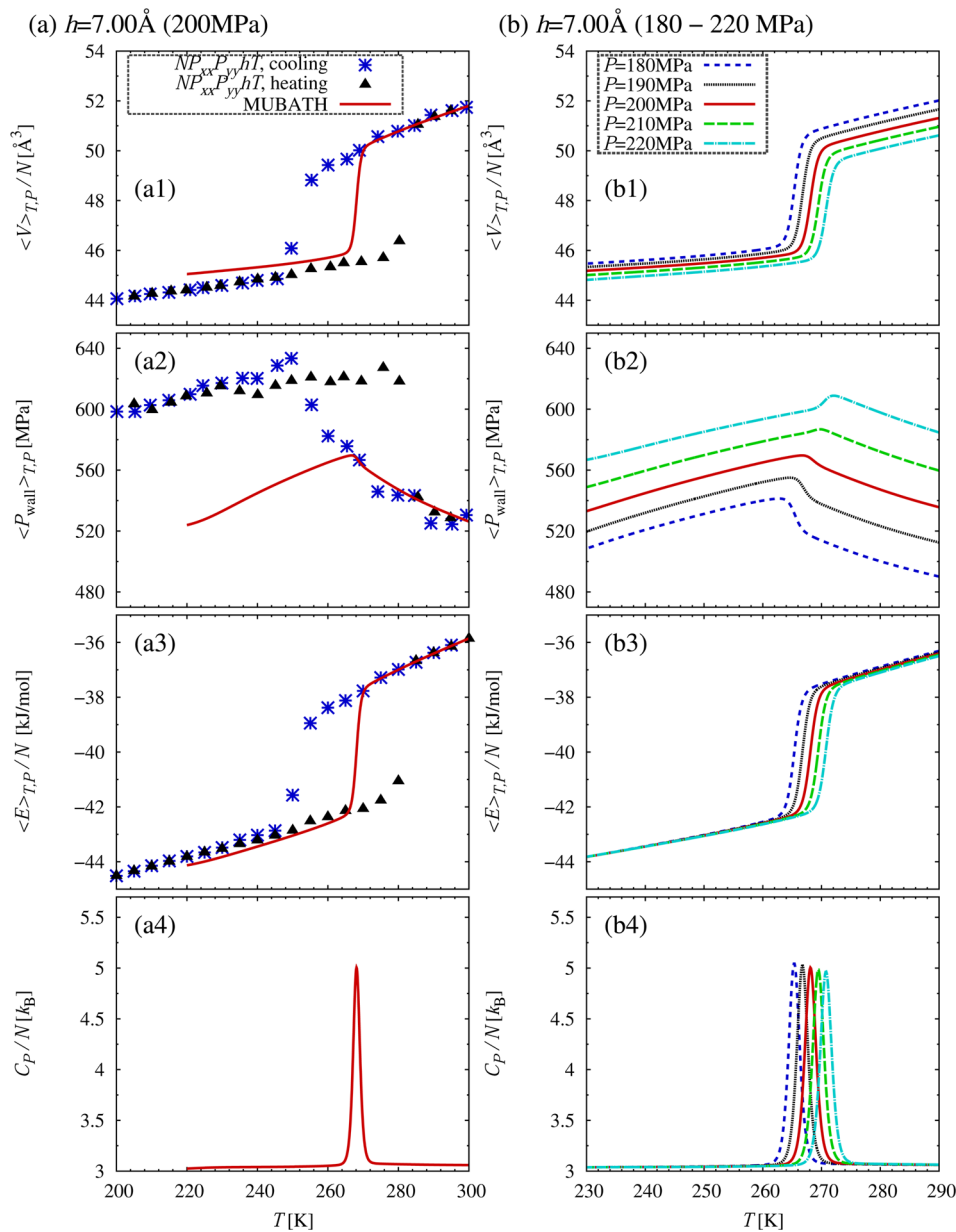


Figure 6. Results for $h = 7.0 \text{ \AA}$. For details, see the caption of Figure 3.

$$\left(\frac{\partial T}{\partial h}\right)_{p_{xx}} = -\frac{T[(a\Delta P)^L - (a\Delta P)^S]}{u^L - u^S + (a^L - a^S)h p_{xx}} \quad (29)$$

where u^L and u^S denote the internal energy of the liquid and solid phase, respectively, a^L and a^S denote the simulation cell area of the liquid and solid phase, respectively, and $\Delta P = P_{zz} - P_{xx}$. The calculated value of $(\partial T/\partial P_{xx})_h$ and $(\partial T/\partial h)_{p_{xx}}$ are summarized in Figure 8a and b, respectively. In Figure 8, the results of cooling/heating simulations are also plotted as a reference data. The phase diagram in Figure 8c is valid in thermodynamics, as it is consistent with $(\partial T/\partial h)_{p_{xx}}$ in Figure 8b.

For $h \leq 6.2 \text{ \AA}$ the computed liquid-to-solid transition temperatures are nearly a constant (240–250 K), independent of h . This is supported by $(\partial T/\partial h)_{p_{xx}} \sim 0$ in Figure 8b. Note that the equilibrium temperature between ice Ih and water at 200 MPa is ~ 202 K using the TIP4P model.³⁸ Therefore, the equilibrium temperatures of HD-RMIs are higher than those of bulk ice Ih, on basis of the TIP4P model. For $6.2 \text{ \AA} \leq h \leq 7.2 \text{ \AA}$,

a maximum is observed around $h = 7.0 \text{ \AA}$. The sign change for $(\partial T/\partial h)_{p_{xx}}$ from positive to negative at $h \sim 7.0 \text{ \AA}$ in Figure 8b also indicates the existence of a maximum. Note that Koga and Tanaka¹⁹ computed the freezing/melting temperatures for $h \geq 6.24 \text{ \AA}$ without using the Ewald summation, and they also observed a maximum in the freezing/melting temperature. In Figure 8c, one can see that, at a constant temperature ($T \sim 260$ K), the “liquid \rightarrow HD-RMI \rightarrow liquid” transition occurs. Indeed, Zangi and Mark¹⁷ observed “monolayer liquid \rightarrow HD-RMI \rightarrow bilayer liquid” transition by increasing the slit width h at a constant pressure and temperature.

The liquid-to-solid transition temperature within the pressure range $180 \text{ MPa} \leq P \leq 220 \text{ MPa}$ is also determined based on the peak of the heat capacity curve in b4 of Figures 3–7 and the pressure–temperature phase diagram at constant h is summarized in Figure 9. The liquid-to-solid transition conditions agree quantitatively with $(\partial T/\partial P_{xx})_h$ in Figure 8a. It is confirmed that the liquid-to-solid transition temperature exhibits a maximum

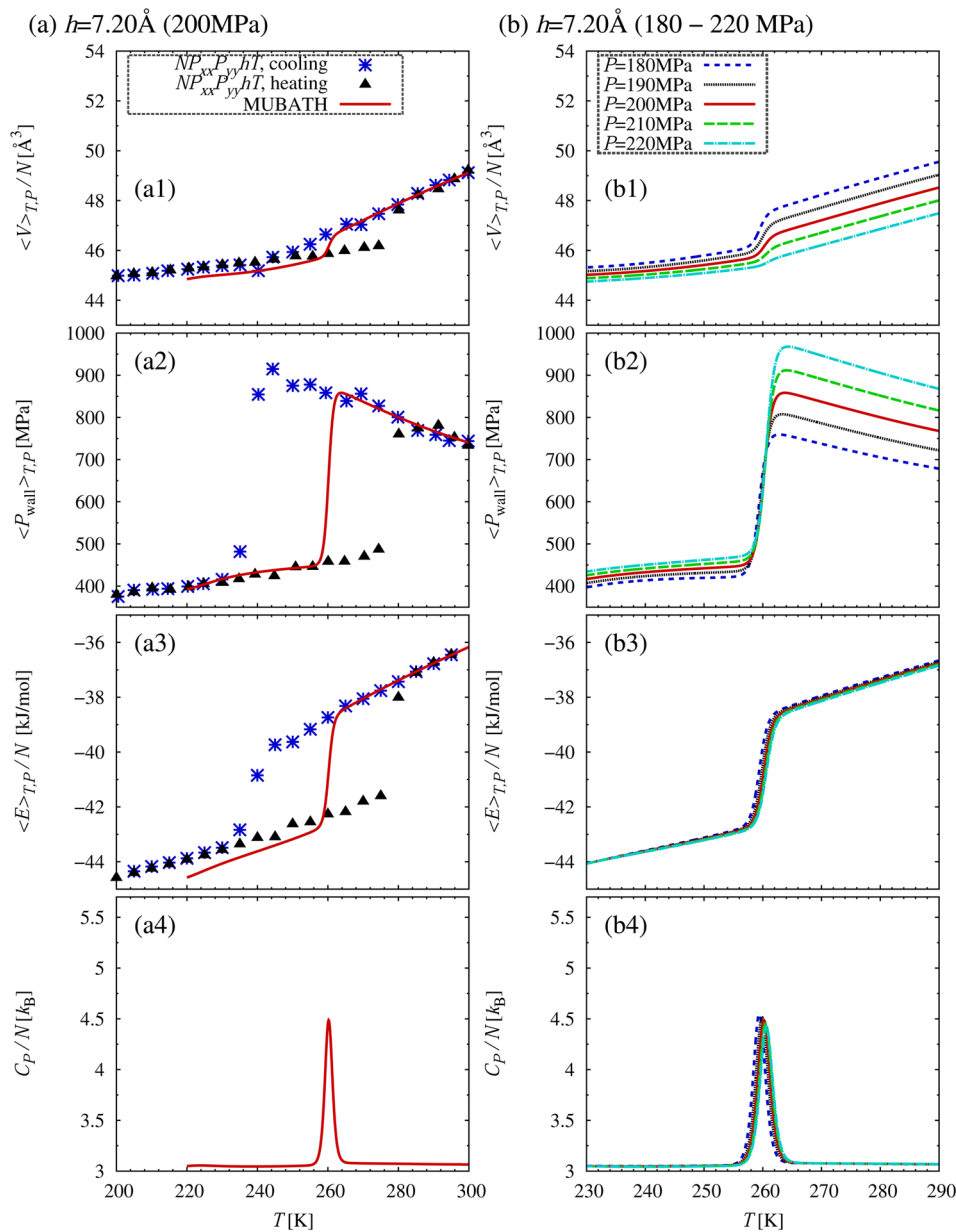


Figure 7. Results at $h = 7.2 \text{ \AA}$. For details, see the caption of Figure 3.

around $h = 7.0 \text{ \AA}$. For $h \geq 7.3 \text{ \AA}$, HD-RMI is not observed; rather, a monolayer amorphous ice is observed. To clarify whether this is an amorphous ice or another 2D crystal structure, extensive simulations of larger systems will be required. Thus far, the MUBATH simulation has not been applied to large systems due to the difficulty in determining MUBATH weight factor. Further methodology advance is required to address this issue. Note also that low-density 4·8² monolayer ice²¹ is not observed in our TIP4P simulations.

4.3. High Density Puckered and Flat Monolayer Ice. In a previous section, we show that the liquid-to-solid transition temperatures are nearly a constant for $h \leq 6.2 \text{ \AA}$ but there exists a maximum between $h = 6.2 \text{ \AA}$ and $h = 7.2 \text{ \AA}$. To gain more insights into the liquid-to-solid transition for water confined to a slit nanopore, we focus on the ice structures for $h = 7.00 \text{ \AA}$ and $h = 5.40 \text{ \AA}$. Figure 10 displays snapshots of monolayer ices for $h = 7.00 \text{ \AA}$ and $h = 5.40 \text{ \AA}$ at $P_{xx} = P_{yy} = 200 \text{ MPa}$ and $T = 165 \text{ K}$ in the cooling simulations. A top view of the 2D ices

[see Figure 10] shows that both 2D ices exhibit the same rhombic structure. However, a side view shows that the two ices look very different, one exhibits puckered structure whereas the other is very flat. In Figure 10, we name (a) the high-density puckered rhombic monolayer ice (HD-pRMI) and (b) the high-density flat rhombic monolayer ice (HD-fRMI). Note that HD-pRMI has been predicted from previous simulations^{17–19,21} while HD-fRMI has not been reported in the literature.

More detailed structural differences between HD-pRMI and HD-fRMI can be seen from the computed density profiles and lateral radial distribution functions of oxygen atoms (in NVT ensemble) for given h . The starting configuration is the structure at $T = 165 \text{ K}$ and $P_{xx} = 200 \text{ MPa}$. Here, the lateral radial distribution function is given by

$$g_{\text{O-O:2D}}(r) = \frac{\langle n_{2\text{D}}(r) \rangle}{2\pi r^2 dr \rho_{2\text{D}}} \quad (30)$$

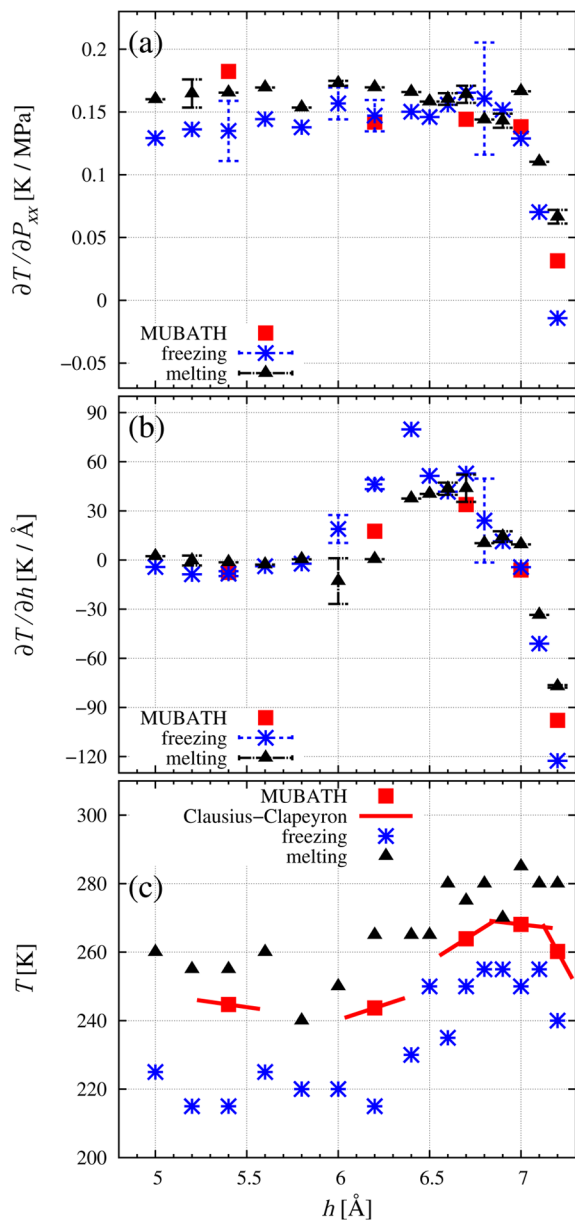


Figure 8. (a) $(\partial T / \partial P_{xx})_h$ calculated by eq 28, (b) $(\partial T / \partial h)_{P_{xx}}$ calculated by eq 29, and (c) the liquid-to-solid transition temperatures $T(h, P_{xx})$. The results of cooling/heating simulations from conventional isobaric–isothermal ensembles are also presented.

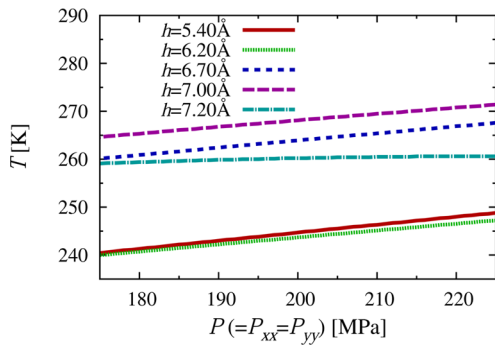


Figure 9. Pressure–temperature phase diagram for constant h . The liquid-to-solid transition lines are determined based on the peaks of the heat capacity curves in b4 of Figures 3–7.

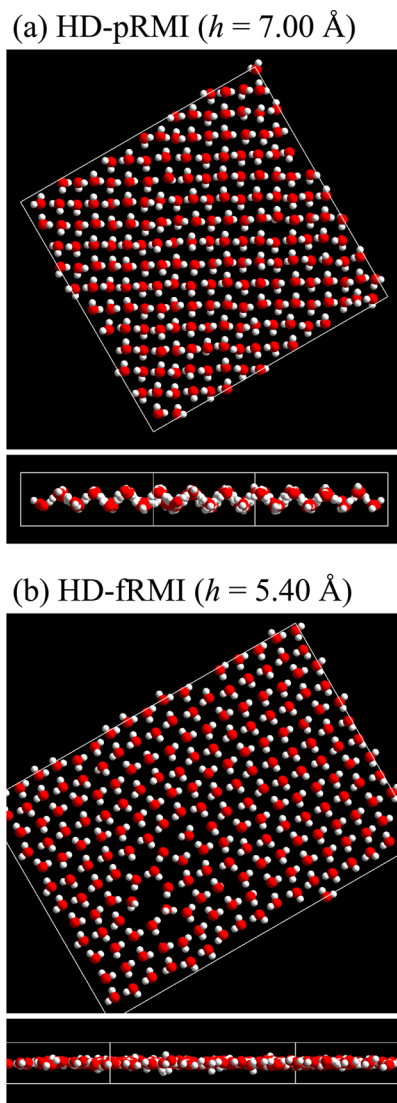


Figure 10. Monolayer ice structures at $P_{xx} = P_{yy} = 200$ MPa and $T = 165$ K in cooling simulations in the $NP_{xx}P_{yy}hT$ ensemble. (a) High-density puckered rhombic monolayer ice (HD-pRMI) for $h = 7.00$ Å and (b) high-density flat rhombic monolayer ice (HD-fRMI) for $h = 5.40$ Å.

where $r = (x^2 + y^2)^{1/2}$, $n_{2D}(r)$ is the number of oxygen in the differential space between r and $r + dr$, and $\rho_{2D} = N/(L_x L_y)$ is an areal density. The density profiles are displayed in Figure 11. A single peak is observed for $h \leq 5.8$ Å, whereas a double peak is observed for $h \geq 6.2$ Å. It is confirmed that HD-pRMI can gradually become HD-fRMI by reducing the slit width h . The lateral radial distribution functions are displayed in Figure 12. At $r = 2–3$ Å, a single peak is observed for $h \leq 6.2$ Å, whereas a double peak is observed for $h \geq 6.6$ Å. A double peak in $g_{O-O;2D}(r)$ at $r = 2–3$ Å is a characteristic of HD-pRMI (see Figure 3b of ref 19). We confirm that the HD-pRMI is the same as that previously reported. In Figure 12, it is also confirmed that HD-pRMI can gradually become HD-fRMI by reducing the slit width h . As the HD-pRMI shows a double peak in its density profile (Figure 11), the HD-pRMI should have an intralayer thickness. Thus, there should exist an appropriate h that fits the thickness nicely. We find that the appropriate h is around 7.0 Å, for which the HD-pRMI is very easy to form and where a maximum in the liquid-to-solid

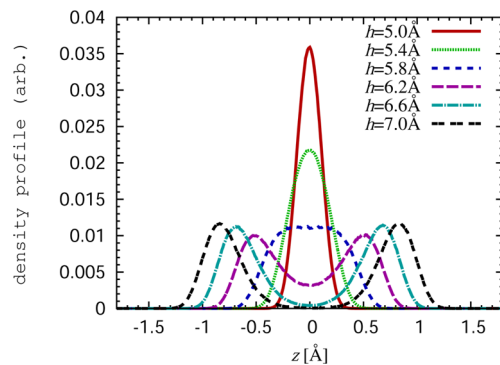


Figure 11. Density profiles of oxygen atoms of monolayer ices, calculated in the NVT ensemble and starting from the structure at $T = 165\text{ K}$ and $P_{xx} = 200\text{ MPa}$.

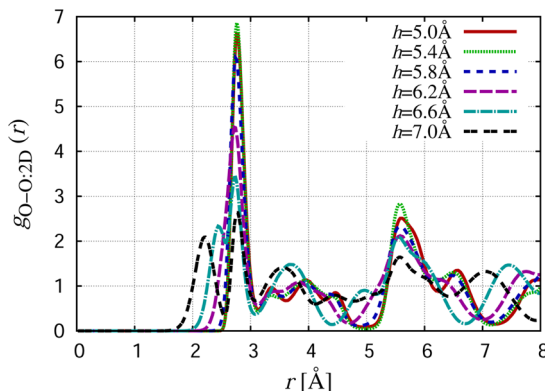


Figure 12. Lateral radial distribution functions [eq 30], calculated in the NVT ensemble and starting from the structure at $T = 165\text{ K}$ and $P_{xx} = 200\text{ MPa}$.

transition temperature versus h arises. On the other hand, the HD-fRMI shows a single peak in its density profile (Figure 11). So HD-fRMI can be viewed as a completely flat monolayer ice. As long as h is sufficiently narrow to just accommodate HD-fRMI, h should have little effect on the liquid-to-solid temperature (the freezing point).

The potential energy due to water–water interaction and water–wall interaction is summarized in Figure 13. No sharp

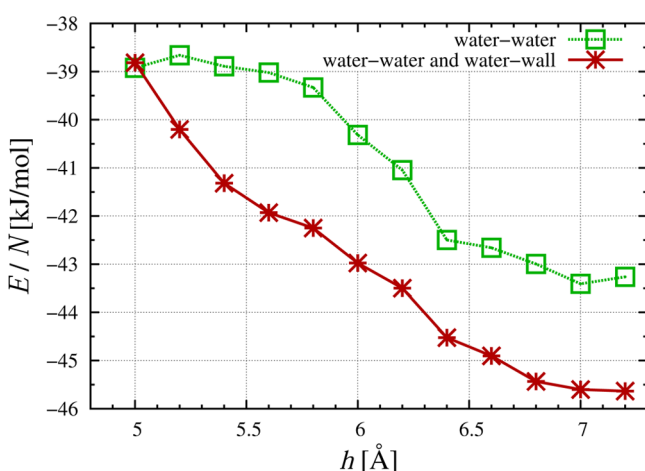


Figure 13. Potential energy due to the water–water interaction and the water–wall interaction for the HD-RMIs, calculated in NVT ensemble and starting from the structure at $T = 165\text{ K}$ and $P_{xx} = 200\text{ MPa}$.

change in potential energy between HD-pRMI and HD-fRMI is observed. The gradual structural change and the continuous potential energy change between TIP4P HD-pRMI and TIP4P HD-fRMI imply that they are not distinct ice phases. It will be interesting to investigate in future whether the phase change from the TIP4P HD-fRMI to HD-pRMI is a continuous transition^{8,16} or a very weak first-order transition as the slit width h is enlarged stepwise within the range $h = 5.4\text{--}6.6\text{ \AA}$.

5. CONCLUSION

We derive a new equation of motion for the implementation of an anisotropic pressure control in multibaric–multithermal ensembles. The new computational approach is applied to compute liquid–solid phase equilibria of TIP4P water confined between two parallel walls with the separation of h . For $h = 5.4\text{ \AA}$, 6.2 \AA , 6.7 \AA , 7.0 \AA , and 7.2 \AA , the liquid-to-solid transition temperatures and pressures are computed quantitatively. For $5.0\text{ \AA} \leq h \leq 6.2\text{ \AA}$, a high-density flat rhombic monolayer ice (HD-fRMI) is observed, while for $6.2\text{ \AA} \leq h \leq 7.2\text{ \AA}$, a high-density puckered rhombic monolayer ice (HD-pRMI) is observed. We find that the liquid-to-solid transition temperature of HD-pRMI shows a maximum for $h \sim 7.0\text{ \AA}$, consistent with the conclusion from a previous simulation by Koga and Tanaka. We also find that the liquid-to-solid transition temperature of HD-fRMI is insensitive to the slit width h because HD-fRMI is a strictly flat monolayer ice. Finally, we find that the HD-pRMI can be gradually transformed into HD-fRMI by reducing the slit width h . The phase change from the flat TIP4P monolayer ice to the puckered TIP4P monolayer ice occurs within $h = 5.4\text{--}6.6\text{ \AA}$. It will be interesting to investigate in future whether the phase change from the TIP4P HD-fRMI to HD-pRMI is a continuous transition^{8,16} or a very weak first-order transition as the slit width h is enlarged in very small steps in the range of $h = 5.4\text{--}6.6\text{ \AA}$.

■ AUTHOR INFORMATION

Corresponding Author

*E-mail: yasuoka@mech.keio.ac.jp; xzeng1@unl.edu.

Notes

The authors declare no competing financial interest.

■ ACKNOWLEDGMENTS

T.K. is supported by Grant in Aid for Japan Society for the Promotion of Science (JSPS) Fellows 23-2003 of the Ministry of Education, Culture, Sports, Science, and Technology (MEXT) in Japan. A.M. is supported by Grant in Aid for Scientific Research on Innovative Areas “Material Design through Computations” from the MEXT in Japan. X.C.Z. is supported by grants from the National Science Foundation (CBET-1066947), the U.S. Army Research Laboratory (W911NF1020099), and the Nebraska Research Initiative.

■ REFERENCES

- (1) England, J. L.; Lucent, D.; Pande, V. S. *J. Am. Chem. Soc.* **2008**, *130*, 11838–11839.
- (2) Fadda, E.; Woods, R. J. *J. Chem. Theory Comput.* **2011**, *7*, 3391–3398.
- (3) Manzano, H.; Moeini, S.; Marinelli, F.; van Duin, A. C. T.; Ulm, F.-J.; Pellenq, R. J. M. *J. Am. Chem. Soc.* **2012**, *134*, 2208–2215.
- (4) Pitman, M. C.; van Duin, A. C. T. *J. Am. Chem. Soc.* **2012**, *134*, 3042–3053.
- (5) Li, H.; Zeng, X. C. *J. Chem. Theory Comput.* **2012**, *8*, 3034–3043.

- (6) Sulpizi, M.; Gaigeot, M.-P.; Sprik, M. *J. Chem. Theory Comput.* **2012**, *8*, 1037–1047.
- (7) Koga, K.; Parra, R. D.; Tanaka, H.; Zeng, X. C. *J. Chem. Phys.* **2000**, *113*, 5037–5040.
- (8) Koga, K.; Gao, G. T.; Tanaka, H.; Zeng, X. C. *Nature* **2001**, *412*, 802–805.
- (9) Maniwa, Y.; Kataura, H.; Abe, M.; Ueda, A.; Suzuki, S.; Achiba, Y.; Kira, H.; Matsuda, K.; Kadokawa, H.; Okabe, Y. *Chem. Phys. Lett.* **2005**, *401*, 534–538.
- (10) Bai, J.; Wang, J.; Zeng, X. C. *Proc. Natl. Acad. Sci. U.S.A.* **2006**, *103*, 19664–19667.
- (11) Byl, O.; Liu, J.-C.; Wang, Y.; Yim, W.-L.; Johnson, J. K.; John T. Yates, J. *J. Am. Chem. Soc.* **2006**, *128*, 12090–12097.
- (12) Takaiwa, D.; Hatano, I.; Koga, K.; Tanaka, H. *Proc. Natl. Acad. Sci. U.S.A.* **2008**, *105*, 39–43.
- (13) Kyakuno, H.; Matsuda, K.; Yahiro, H.; Fukuoka, T.; Miyata, Y.; Yanagi, K.; Maniwa, Y.; Kataura, H.; Saito, T.; Yumura, M.; Iijima, S. J. *Phys. Soc. Jpn.* **2010**, *79*, 083802.
- (14) Koga, K.; Zeng, X. C.; Tanaka, H. *Phys. Rev. Lett.* **1997**, *79*, S262.
- (15) Koga, K.; Tanaka, H.; Zeng, X. C. *Nature* **2000**, *408*, 564–567.
- (16) Han, S.; Choi, M. Y.; Kumar, P.; Stanley, H. E. *Nat. Phys.* **2010**, *6*, 685–689.
- (17) Zangi, R.; Mark, A. E. *Phys. Rev. Lett.* **2003**, *91*, 025502.
- (18) Kumar, P.; Buldyrev, S.; Starr, F.; Giovambattista, N.; Stanley, H. *Phys. Rev. E* **2005**, *72*, 051503.
- (19) Koga, K.; Tanaka, H. *J. Chem. Phys.* **2005**, *122*, 104711.
- (20) Kimmel, G. A.; Matthiesen, J.; Baer, M.; Mundy, C. J.; Petrik, N. G.; Smith, R. S.; Dohnalek, Z.; Kay, B. D. *J. Am. Chem. Soc.* **2009**, *131*, 12838–12844.
- (21) Bai, J.; Angell, C. A.; Zeng, X. C. *Proc. Natl. Acad. Sci. U.S.A.* **2010**, *107*, 5718–5722.
- (22) Ferguson, A. L.; Giovambattista, N.; Rossky, P. J.; Panagiotopoulos, A. Z.; Debenedetti, P. G. *J. Chem. Phys.* **2012**, *137*, 144501.
- (23) Bai, J.; Zeng, X. C. *Proc. Natl. Acad. Sci. U.S.A.* **2012**, *109*, 21240–21245.
- (24) Schreiber, A.; Ketelsen, I.; Findenegg, G. *Phys. Chem. Chem. Phys.* **2001**, *3*, 1185–1195.
- (25) Morishige, K.; Iwasaki, H. *Langmuir* **2003**, *19*, 2808–2811.
- (26) Tombari, E.; Salvetti, G.; Johari, G. P. *J. Phys. Chem. C* **2012**, *116*, 2702–2709.
- (27) Sliwinska-Bartkowiak, M.; Jazdzewska, M.; Huang, L. L.; Gubbins, K. E. *Phys. Chem. Chem. Phys.* **2008**, *10*, 4909–4919.
- (28) Iiyama, T.; Nishikawa, K.; Suzuki, T.; Kaneko, K. *Chem. Phys. Lett.* **1997**, *274*, 152–158.
- (29) Sliwinska-Bartkowiak, M.; Dudziak, G.; Sikorski, R.; Gras, R.; Gubbins, K.; Radhakrishnan, R. *Phys. Chem. Chem. Phys.* **2001**, *3*, 1179–1184.
- (30) Iiyama, T.; Ruike, M.; Kaneko, K. *Chem. Phys. Lett.* **2000**, *331*, 359–364.
- (31) Ohba, T.; Kaneko, K. *J. Phys. Chem. C* **2007**, *111*, 6207–6214.
- (32) Cao, Z.; Peng, Y.; Yan, T.; Li, S.; Li, A.; Voth, G. A. *J. Am. Chem. Soc.* **2010**, *132*, 11395–11397.
- (33) Tao, Y.; Muramatsu, H.; Endo, M.; Kaneko, K. *J. Am. Chem. Soc.* **2010**, *132*, 1214+.
- (34) Ohba, T.; Kaneko, K. *Langmuir* **2011**, *27*, 7609–7613.
- (35) Mashayak, S. Y.; Aluru, N. R. *J. Chem. Theory Comput.* **2012**, *8*, 1828–1840.
- (36) Wang, S. K. *Handbook of Air Conditioning and Refrigeration*, 1st ed.; McGraw-Hill, 1993; Chapter 25. Thermal Storage and Desiccant Cooling.
- (37) Nomura, T.; Okinaka, N.; Akiyama, T. *Mater. Chem. Phys.* **2009**, *115*, 846–850.
- (38) Koyama, Y.; Tanaka, H.; Gao, G. T.; Zeng, X. C. *J. Chem. Phys.* **2004**, *121*, 7926–7931.
- (39) Wang, J.; Yoo, S.; Bai, J.; Morris, J. R.; Zeng, X. C. *J. Chem. Phys.* **2005**, *123*, 036101.
- (40) Okumura, H.; Okamoto, Y. *Chem. Phys. Lett.* **2004**, *391*, 248–253.
- (41) Okumura, H.; Okamoto, Y. *J. Comput. Chem.* **2006**, *27*, 379–395.
- (42) Berg, B. A. *Fields Inst. Commun.* **2000**, *26*, 1–24, DOI: arXiv:cond-mat/9909236v1.
- (43) Mitsutake, A.; Sugita, Y.; Okamoto, Y. *Biopolymers* **2001**, *60*, 96–123.
- (44) Mitsutake, A.; Mori, Y.; Okamoto, Y. In *Biomolecular Simulations: Methods and Protocols*; Monticelli, L., Salonen, E., Eds.; Humana Press: New York, 2012; pp 153–195, arXiv:1012.5726.
- (45) Mitsutake, A.; Okamoto, Y. *Phys. Rev. E* **2009**, *79*, 047701.
- (46) Mitsutake, A.; Okamoto, Y. *J. Chem. Phys.* **2009**, *130*, 214105.
- (47) Muguruma, C.; Okamoto, Y. *Phys. Rev. E* **2008**, *77*, 051201.
- (48) Kaneko, T.; Mitsutake, A.; Yasuoka, K. *J. Phys. Soc. Jpn.* **2012**, *81*, SA014.
- (49) Okumura, H.; Okamoto, H. *J. Phys. Soc. Jpn.* **2004**, *73*, 3304–3311.
- (50) Kaneko, T.; Akimoto, T.; Yasuoka, K.; Mitsutake, A.; Zeng, X. C. *J. Chem. Theory Comput.* **2011**, *7*, 3083–3087.
- (51) Parrinello, M.; Rahman, A. *J. Appl. Phys.* **1981**, *52*, 7182–7190.
- (52) Ilnytskyi, J. M.; Wilson, M. R. *Comput. Phys. Commun.* **2002**, *148*, 43–58.
- (53) Jorgensen, W. L.; Chandrasekhar, J.; Madura, J. D.; Impey, R. W.; Klein, M. L. *J. Chem. Phys.* **1983**, *76*, 926–935.
- (54) Lee, S. H.; Rossky, P. J. *J. Chem. Phys.* **1994**, *100*, 3334–3345.
- (55) Ghoufi, A.; Morineau, D.; Lefort, R.; Hureau, I.; Hennous, L.; Zhu, H.; Szymczyk, A.; Malfreyt, P.; Maurin, G. *J. Chem. Phys.* **2011**, *134*, 074104.
- (56) Eslami, H.; Mozaffari, F.; Moghadasi, J.; Mueller-Plathe, F. *J. Chem. Phys.* **2008**, *129*, 194702.
- (57) Okumura, H.; Okamoto, Y. *Phys. Rev. E* **2004**, *70*, 026702.
- (58) Wang, F.; Landau, D. P. *Phys. Rev. Lett.* **2001**, *86*, 2050–2053.